

## Spinel-based ceramic membranes coupling solid sludge recycling with oily wastewater treatment

Chen, Mingliang; Zhu, Li; Chen, Jingwen; Yang, Fenglin; Tang, Chuyang Y.; Guiver, Michael D.; Dong, Yingchao

**DOI**

[10.1016/j.watres.2019.115180](https://doi.org/10.1016/j.watres.2019.115180)

**Publication date**

2020

**Document Version**

Accepted author manuscript

**Published in**

Water Research

**Citation (APA)**

Chen, M., Zhu, L., Chen, J., Yang, F., Tang, C. Y., Guiver, M. D., & Dong, Y. (2020). Spinel-based ceramic membranes coupling solid sludge recycling with oily wastewater treatment. *Water Research*, 169, Article 115180. <https://doi.org/10.1016/j.watres.2019.115180>

**Important note**

To cite this publication, please use the final published version (if applicable).  
Please check the document version above.

**Copyright**

Other than for strictly personal use, it is not permitted to download, forward or distribute the text or part of it, without the consent of the author(s) and/or copyright holder(s), unless the work is under an open content license such as Creative Commons.

**Takedown policy**

Please contact us and provide details if you believe this document breaches copyrights.  
We will remove access to the work immediately and investigate your claim.

# Supporting information

## Spinel-based Ceramic Membranes Coupling Solid Sludge Recycling with Oily Wastewater Treatment

Mingliang Chen<sup>a,b</sup>, Li Zhu<sup>c</sup>, Jingwen Chen<sup>a</sup>, Fenglin Yang<sup>a</sup>, Chuyang Y. Tang<sup>d</sup>, Michael D. Guiver<sup>e</sup>, Yingchao Dong<sup>a,\*</sup>

<sup>a</sup>Key Laboratory of Industrial Ecology and Environmental Engineering (Ministry of Education, MOE), School of Environmental Science and Technology, Dalian University of Technology, Dalian 116024, China

<sup>b</sup>Department of Sanitary Engineering, Faculty of Civil Engineering and Geosciences, Delft University of Technology, P.O. Box 5048, 2600 GA Delft, The Netherlands

<sup>c</sup>Engineering Research Center of Environmental Materials and Membrane Technology of Hubei province, School of Materials Science and Engineering, Wuhan Institute of Technology, Wuhan, P. R. China

<sup>d</sup>Department of Civil Engineering, The University of Hong Kong, Pokfulam, Hong Kong S.A.R., China

<sup>e</sup>State Key Laboratory of Engines, and Collaborative Innovation Center of Chemical Science and Engineering (Tianjin), Tianjin University, Tianjin 300072, P R China

### ***Corresponding authors:***

Dr. Yingchao Dong, Professor  
Key Laboratory of Industrial Ecology and Environmental Engineering (Ministry of Education, MOE),  
School of Environmental Science and Technology, Dalian University of Technology, Dalian 116024,  
China  
Tel: +86-411-84706328 E-mail: [ycdong@dlut.edu.cn](mailto:ycdong@dlut.edu.cn)

## 28 S1. Preparation of hollow fiber ceramic membranes

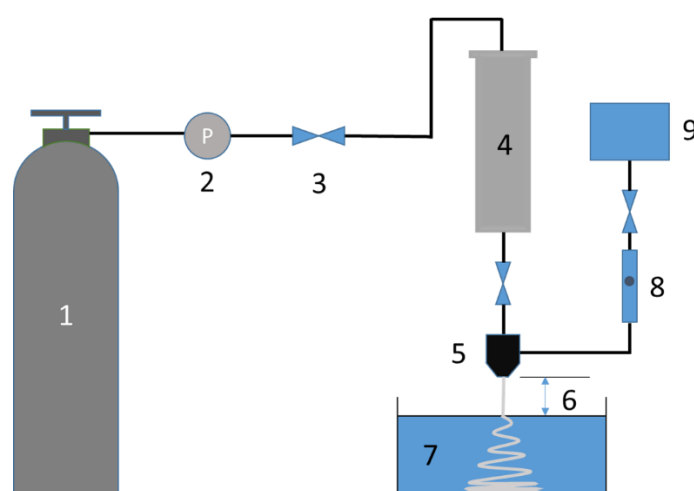
29 **Table S1**

30 Chemical composition (wt. %) of calcined bauxite measured by semi-quantitative XRF

Materials	Chemical composition (wt. %)										
	Al <sub>2</sub> O <sub>3</sub>	SiO <sub>2</sub>	TiO <sub>2</sub>	Fe <sub>2</sub> O <sub>3</sub>	MgO	CaO	K <sub>2</sub> O	SO <sub>3</sub>	P <sub>2</sub> O <sub>5</sub>	Na <sub>2</sub> O	others
Calcined bauxite	83.49	8.76	3.54	2.30	0.14	0.17	0.06	0.05	0.20	0.14	0.07

31 The loss on ignition of calcined bauxite is 1.09 wt. %

### 32 S1.1. Membrane fabrication



33  
34 **Fig. S1.** Schematic diagram of experimental set-up for dry-wet spinning fabrication of hollow fiber  
35 membrane (1. Nitrogen cylinder, 2. Pressure gauge, 3. Valve, 4. Stainless reservoir, 5. Spinneret, 6. Air  
36 gap, 7. External coagulant, 8. Rotameter, 9. Internal coagulant)

37 The spinel-based HFCMs were prepared by a dry-wet spinning technique (Fig. S1),  
38 involving immersion-induced phase inversion and drying-sintering processes. Polyethersulfone  
39 (PES) was first dissolved in N-methyl-2-pyrrolidone (NMP) solvent at a PES/ NMP mass ratio  
40 of 1/4, then 3 g (1.5 wt. %) polyvinylpyrrolidone (PVP), moderating the solution viscosity, was  
41 added into the polymer solution under vigorous stirring for 6 h until a homogenous polymer  
42 mixture solution was formed. The ball-milled bauxite and nickel oxide mixture powder, based  
43 on a molar ratio of Ni/Al = 1/4, were added into the polymer solution and then wet-ball-milled  
44 for 48 h to ensure that the ceramic powders were well-dispersed. A molar ratio of Ni/Al = 1/2

45 was studied to semi-quantitatively analyze each phase content present in the samples. The  
 46 prepared suspensions were then transferred to a gas tight reservoir and degassed under vacuum  
 47 for 30 min at room temperature (25 °C).

48 The degassed spinning suspension was immediately introduced into a stainless steel  
 49 reservoir and subsequently pressurized with nitrogen gas, and then the fiber was extruded  
 50 through a tube-in-orifice spinneret (outer diameter 2.5 mm, inner diameter 1.3 mm) into  
 51 external coagulant with different air-gap distances. Deionized (DI) water was used the internal  
 52 coagulant at a flow rate of 20 mL·min<sup>-1</sup>. The external coagulants used in this work are the  
 53 mixtures of tap-water and ethanol with different ethanol volumes (0 %, 30 %, 60 % and 90 %)  
 54 (Table S2).

55 **Table S2**

56 Suspension compositions and dry-wet spinning parameters for Fibers 1-8

Fiber no.	Solid state loading (wt.%)	Bore fluid flow rate (mL·min <sup>-1</sup> )	Air-gap (cm)	Internal coagulant	External coagulant (water/ethanol)
1	50	20	15	Deionized water	100/0
2	55	20	15	Deionized water	100/0
3	60	20	15	Deionized water	100/0
4	60	20	10	Deionized water	100/0
5	60	20	3	Deionized water	100/0
6	60	20	15	Deionized water	70/30
7	60	20	15	Deionized water	40/60
8	60	20	15	Deionized water	10/90

57 The hollow fiber green bodies were immersed in the external coagulant bath overnight to  
 58 allow completion of the phase inversion process. They were then rinsed with tap water in order  
 59 to remove trace amounts of NMP. Afterwards, the fibers were dried at room temperature (25 °C),  
 60 then sintered in air for 2 h at temperatures between 1200 °C and 1300 °C with an interval of

61 25 °C to produce robust porous HFCMs.

## 62 *SI.2. Membrane characterization*

63 The tests of three-point bending strength of sintered HFCMs were performed using a  
64 universal testing machine (AGS-X, Shimadzu Ltd., Japan). During the tests, the samples were  
65 placed on a span of 8 mm and were loaded at a crosshead speed of 0.02 mm·min<sup>-1</sup> until fracture  
66 occurred. Each sample were repeated for twenty runs. The bending strength,  $\sigma_f$ , was calculated  
67 from the following equation:

$$68 \quad \sigma_f = 8FLD/(\pi(D^4-d^4)) \quad (1)$$

69 Where, F is the measured force at which fracture takes place (N), L, D and d are the span (8mm),  
70 the outer and inner diameters of the hollow fiber, respectively.

71 Pore size distribution was determined using a pore size distribution analyzer (Porometer  
72 3G, Quantachrome Instruments, USA) based on a gas-liquid displacement method with  
73 nitrogen gas as the permeation medium.

$$74 \quad r = 4\gamma\cos\theta/\Delta P \quad (2)$$

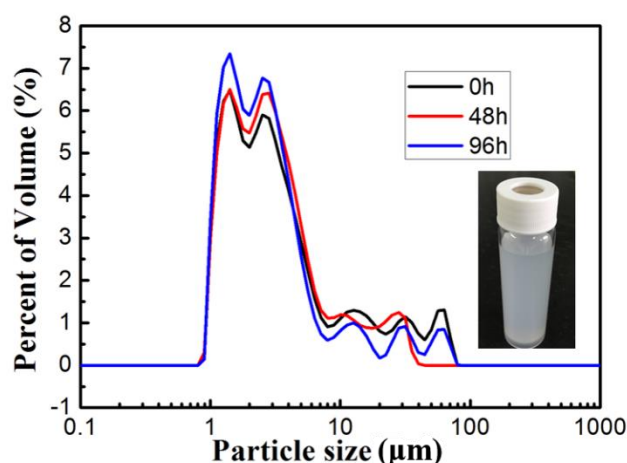
75 where r ( $\mu\text{m}$ ) is the diameter of the pore,  $\Delta P$  (MPa) is the applied pressure difference,  $\gamma$  (mN/m)  
76 is the surface tension of the liquid and  $\theta$  is the contact angle.

77 The Fourier-transform infrared spectroscopy (FTIR) was recorded with an infrared  
78 spectrometer (Bruker EQUINOX55, Germany) to analyze the functional groups present in  
79 sintered spinel-based membranes. The X-ray photoelectron spectroscopy (XPS) measurements  
80 were performed on an electron spectrometer (ESCALAB 250Xi, ThermoFisher, US) for multi-  
81 technique surface analysis systems, with Al K $\alpha$  photons used as a source and operated at a  
82 constant power of 300 W. The core level binding energies of the different peaks were  
83 normalized by setting the bonding energy of C1s peaks for C-C bonds at 284.8 eV. The structure  
84 and morphology of the formed spinel was observed through transmission electron microscopy  
85 (TEM, JEM-2010(HR), JEOL, Japan) operated at 200 kV. To study microtextures, diffraction

86 patterns (DPs) were collected using the selected area electron diffraction (SAED) technique.

87 Pure water flux of the HFCMs was characterized by a laboratory-made crossflow filtration  
88 apparatus. The apparatus was operated at a very low constant trans-membrane pressure of 0.1  
89 bar with different feed velocities ranging from  $0.14 \text{ m}\cdot\text{s}^{-1}$  to  $0.73 \text{ m}\cdot\text{s}^{-1}$ . Before starting the  
90 measurements of permeate flux, all samples were ultrasonically cleaned with ethanol for 5 min.

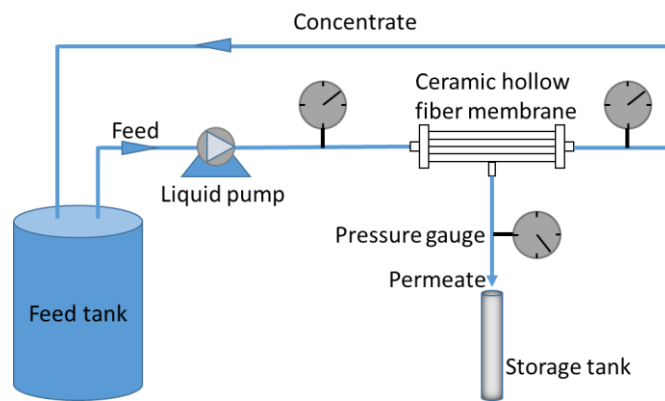
### 91 *S1.3. Stabilization of O/W emulsions*



92  
93 **Fig. S2.** The size distributions of emulsified oil droplets in the feed solutions after 0, 48, and 96 h static  
94 storage.

95 In order to illustrate the stability of O/W emulsions prepared in our work, the size  
96 distributions of emulsified oil droplets after 0, 48, and 96 h static storing were measured using  
97 a laser particle size analyzer, as shown in Fig. S2. It is clear that the prepared O/W emulsions  
98 were highly stable for MF separation experiments, as the size distributions of emulsified oil  
99 droplets are quite similar even after 96 h static storage, indicating a good dispersion and stable  
100 state. In addition, the majority of the size of oil droplets in the emulsions are in the range of  
101  $1\sim 10 \mu\text{m}$ , which meets the classification criteria for industrial O/W emulsified wastewaters.

### 102 *S1.4. O/W emulsion separation by HFCMs*

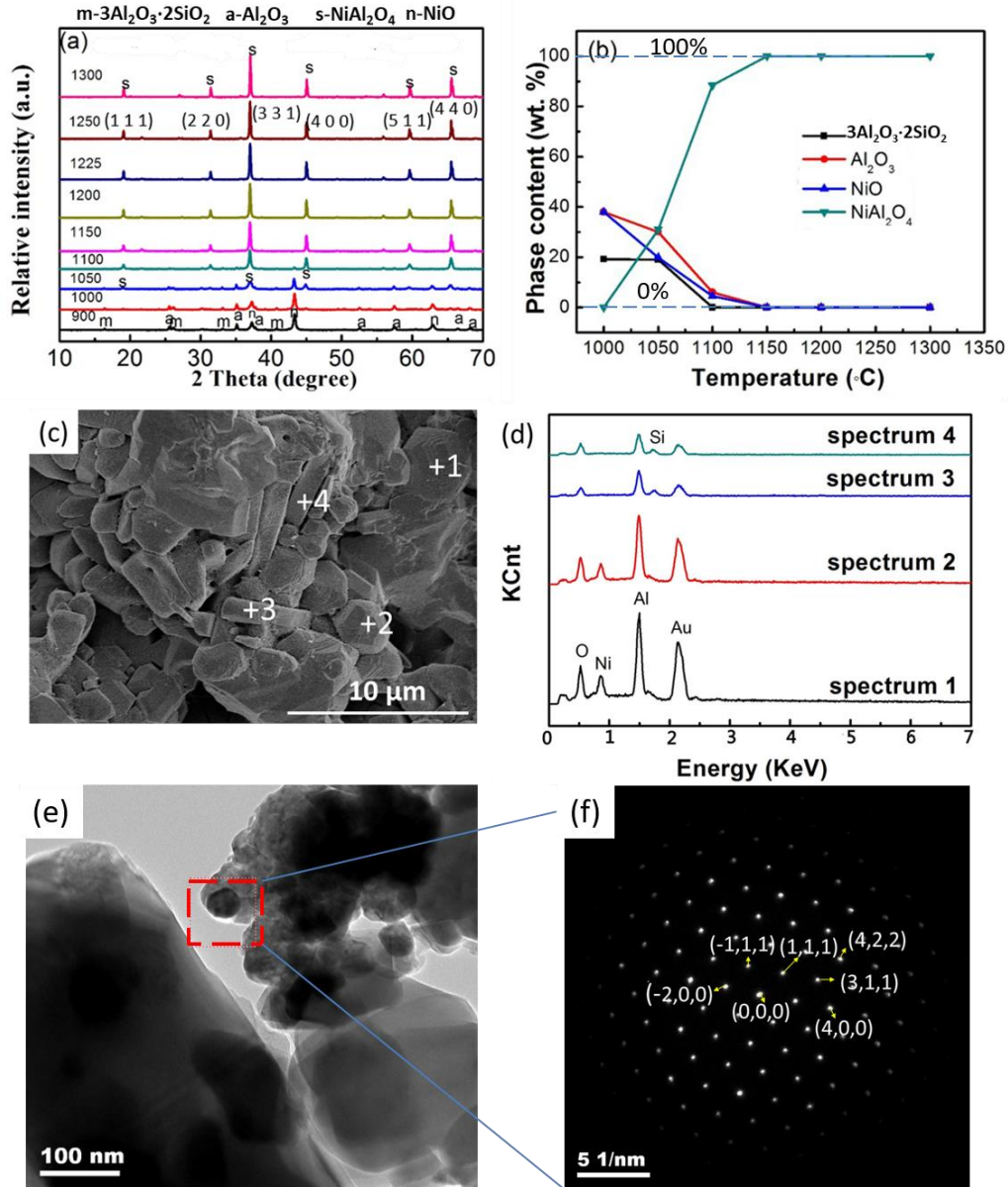


103

104 **Fig. S3.** Schematic diagram of experimental setup for membrane-based process treatment of O/W  
 105 emulsions.

106 **S2 Thermal conversion of  $\text{NiAl}_2\text{O}_4$**

107 *S2.1. Thermal Conversion Mechanism of  $\text{NiAl}_2\text{O}_4$*



108

109 **Fig. S4.** (a) XRD patterns and (b) quantified phase content of the spinel-based hollow fiber ceramic  
 110 membranes ( $\text{NiAl}_2$ ) sintered at various temperature from 900 to 1300 °C for 2 h,  $3\text{Al}_2\text{O}_3\cdot 2\text{SiO}_2$  (PDF  
 111 #83-1881),  $\alpha\text{-Al}_2\text{O}_3$  (PDF#99-0036),  $\text{NiAl}_2\text{O}_4$  (PDF#81-0718) and NiO (PDF#44-1159), (c) SEM image  
 112 and (d) EDS spectra of the spinel-based membrane ( $\text{NiAl}_4$ ) sintered at 1400 °C for 2 h, after 15 wt. %  
 113 HF solution etching for 30 min, (e) TEM image of the spinel-based membrane ( $\text{NiAl}_4$ ) sintered at  
 114 1250 °C, (f) SAED patterns of a spinel crystal with octahedral morphology as indicated by red dash line  
 115 in Fig. S4e.

116

117



118 Table S3

119 EDS analysis of the NiAl<sub>4</sub> membrane sintered at 1400 °C for 2 h after leaching at 15 wt. %

120 HF solution for 30 min.

Position	at. %			Molar ratio		Main phase
	Al	Ni	Si	Al/Si	Al/Ni	
Spectrum1	47.14	20.35	-	-	2.3	spinel
Spectrum2	49.22	18.91	-	-	2.6	spinel
Spectrum3	55.18	-	13.75	4	-	mullite
Spectrum4	50.04	-	12.8	3.9	-	mullite

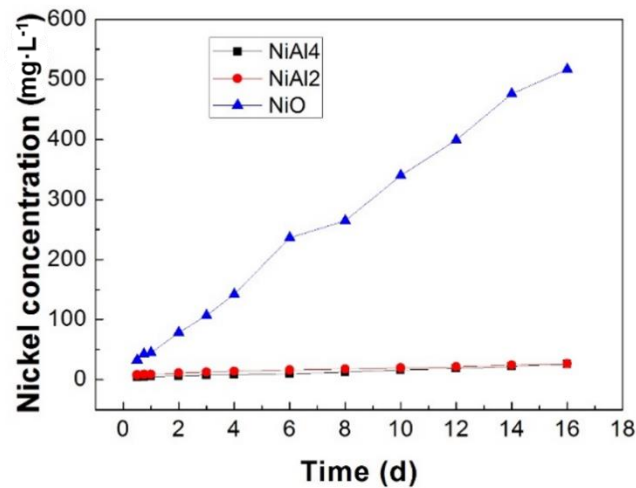
121

## 122 *S2.2. Acidic stability of NiAl<sub>2</sub>O<sub>4</sub>*

123 To evaluate the product leachability under prolonged acidic exposure, the NiO, NiAl<sub>2</sub> and  
124 NiAl<sub>4</sub> samples were tested following a modified method from the U.S. EPA Toxicity  
125 Characteristic Leaching Procedure (TCLP) (Shih and Tang, 2011) by using acetic acid (pH 2.9)  
126 solution as the leaching fluid. Each leaching vial was filled with 40 mL of TCLP extraction  
127 fluid and 2 g of ground powder of NiO and prepared NiAl<sub>2</sub> and NiAl<sub>4</sub> spinel-based HFCMs.  
128 The leachates were filtered through 0.2 μm syringe filters and the concentrations of metal ions  
129 were determined by atomic absorption spectrometer (Solaar M6, Thermo, USA).

130 The stability of NiAl<sub>4</sub> and NiAl<sub>2</sub> phase is much higher than that of NiO (Fig. S5). As  
131 shown, the concentration of leached nickel ion in NiO sample increases sharply with the  
132 leaching time. After 16 days leaching, its nickel ion concentration was as high as 516 mg·L<sup>-1</sup>  
133 and even maintains a rising trend. In contrast, the nickel ion leached from NiAl<sub>2</sub> and NiAl<sub>4</sub> are  
134 found to be much lower than that from NiO. Within 24 h of leaching, its concentration is only  
135 9.17 mg·L<sup>-1</sup> and 5.14 mg·L<sup>-1</sup> and then increases with leaching time very slowly. Even after 16  
136 days leaching, the nickel ion concentration is still very low and the impurity ions from bauxite,  
137 such as titanium and iron ions, are hard to be detected. These results not only illustrate the

138 successful incorporation of nickel into bauxite but also the effective stabilization of nickel into  
 139 the more stable spinel phase  $\text{NiAl}_2\text{O}_4$ , to resist the acidic attack.



140  
 141 **Fig. S5.** Concentration of nickel ion in the NiO and NiAl<sub>2</sub>, NiAl<sub>4</sub> (sintered at 1400 °C) leachates.

142  
 143 **Table S4**

144 Comparison of raw materials for nickel-laden solid state wastes stabilization.

Raw materials	Price (\$/t) <sup>1</sup>	Full transformation temperature (°C)
Bauxite	150-200	1200
Alumina	520-540	1400
Kaolinite	300-360	1350

145 1-adapted from Alibaba.com

146  
 147 **Table S5**

148 Comparison of formation temperature and stability between nickel aluminate spinel phase in  
 149 this work and those reported in the literatures.

Heavy metal	Starting materials	Targeted phase	Formation temperature (°C)	Leachability (mg·L <sup>-1</sup> )	Refs
-------------	--------------------	----------------	----------------------------	------------------------------------	------

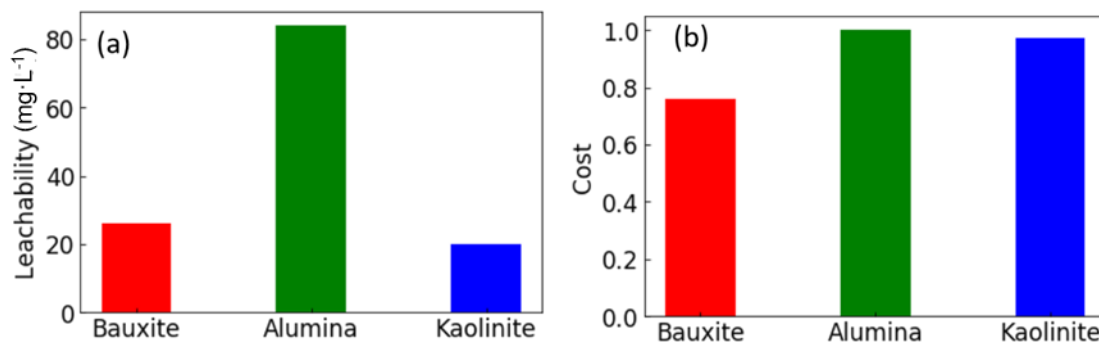
Ni	NiO + bauxite	NiAl <sub>2</sub> O <sub>4</sub>	1000~1200	26	This work
Ni	NiO + $\gamma$ -Al <sub>2</sub> O <sub>3</sub>	NiAl <sub>2</sub> O <sub>4</sub>	1100~1400	84	(Shih et al., 2006b)
Ni	NiO + kaolinite	NiAl <sub>2</sub> O <sub>4</sub>	1150~1400	20	(Shih et al., 2006b)
Cu	CuO + bauxite	CuAl <sub>2</sub> O <sub>4</sub>	900~1060	213	(Li et al., 2015a)
Cu	CuO + mullite	CuAl <sub>2</sub> O <sub>4</sub>	950~1050	<200	(Tang et al., 2011a)
Cu	CuO + kaolin	CuAl <sub>2</sub> O <sub>4</sub>	900~1050	<200	(Tang et al., 2011a)
Zn	ZnO + bauxite	ZnAl <sub>2</sub> O <sub>4</sub>	1000~1300	15	(Li et al., 2015b)
Zn	ZnO + corundum	ZnAl <sub>2</sub> O <sub>4</sub>	850~1350	2.7	(Tang et al., 2011b)

150

151 The formation temperature and stability of nickel aluminate spinel phase prepared in this  
152 work are compared with those reported in the literature, as presented in [Table S4](#). For the  
153 stabilization of the same heavy metals, the stable temperature ranges at which they exist are  
154 close to each other, and are independent of the raw materials used. As both bauxite and kaolinite  
155 transform to mullite and corundum/cristobalite under thermal treatment, silica does not react  
156 with nickel, and the only incorporation mechanism is through the reaction between NiO and  
157 mullite or Al<sub>2</sub>O<sub>3</sub> (Shih et al., 2006b). However, the stability of spinel phase shows slight  
158 differences. For example, the leaching of Cu ions from CuO-bauxite, CuO-mullite and CuO-  
159 kaolinite systems is much higher than that of nickel and zinc spinel due to the relatively lower  
160 stability of copper spinel (Tang et al., 2011a; Dong et al., 2010). The NiAl<sub>2</sub>O<sub>4</sub> spinel phase  
161 stable existence temperature range in this work is quite similar with two other NiAl<sub>2</sub>O<sub>4</sub> spinel  
162 phases reported in the literature and its nickel ion leaching concentration is only 26 mg·L<sup>-1</sup>,

163 even after half a month, which is a little higher than that of the NiO-kaolinite system ( $20 \text{ mg}\cdot\text{L}^{-1}$ )  
164  $^1$ ), but much lower than that of the NiO- $\gamma$ - $\text{Al}_2\text{O}_3$  system ( $84 \text{ mg}\cdot\text{L}^{-1}$ ). The reason is possibly due  
165 to enhanced spinel crystallization and robust grain boundaries promoted by the silica flux in  
166 NiO-kaolinite and NiO-bauxite systems (Shih et al., 2006a). By comparison, both the market  
167 price of bauxite mineral and stable existence temperature of nickel-based spinel are lower than  
168 that of alumina and kaolinite (Table S5), indicating that bauxite is an efficient and cost-effective  
169 material for stabilization of nickel-laden solid-state wastes.

170



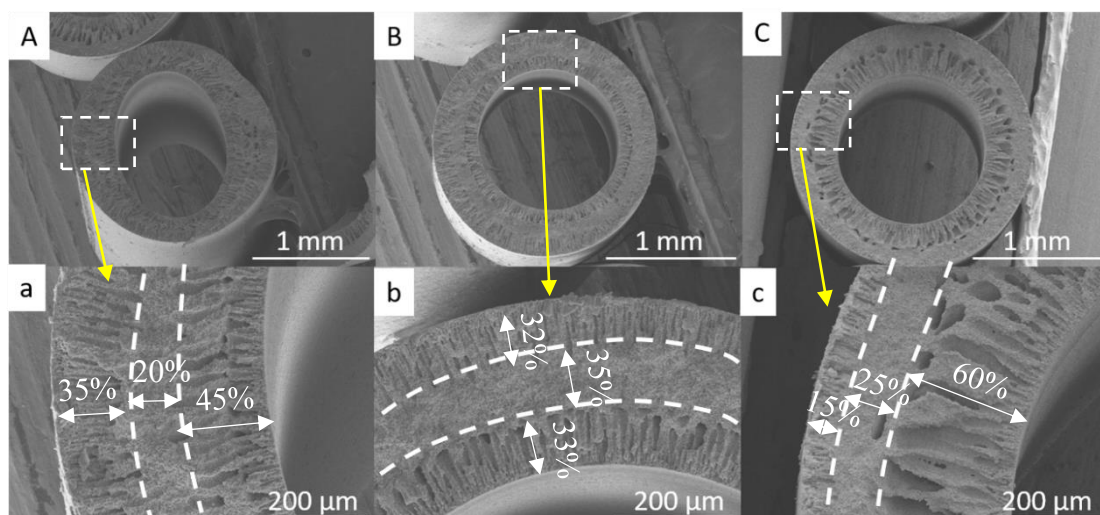
171

172 **Fig. S6.** Acidic leachability (a) and cost comparison (b) of Ni-based spinel stabilized by bauxite  
173 (this work), alumina, and kaolinite, reported in the open literature (Shih et al. 2006b).

174

### 175 **S3. Rational structure design of ceramic membranes**

176 *S3.1. Effect of solid-state loading*

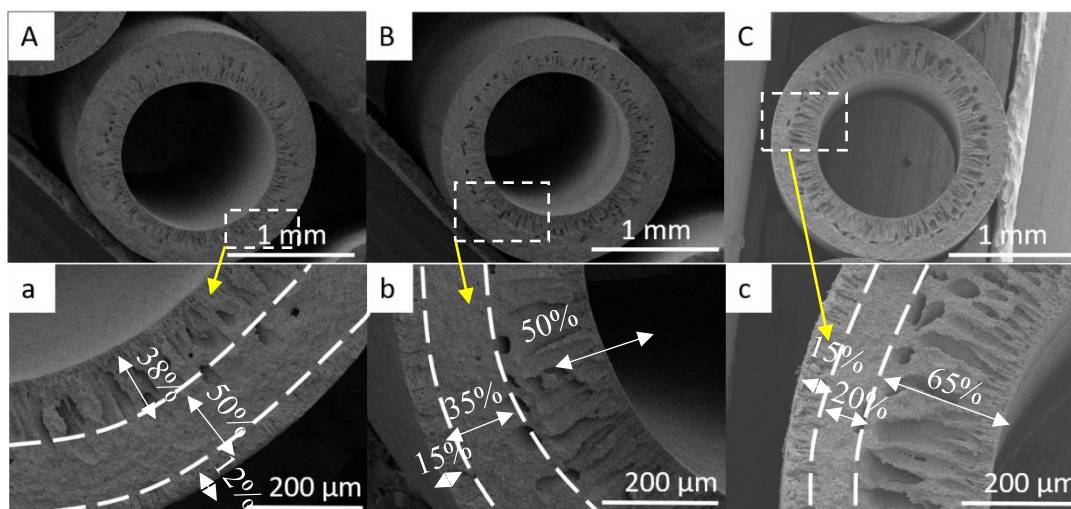


177  
 178 **Fig. S7.** Cross sectional SEM images of fibers 1, fiber 2 and fiber 3 sintered at 1250 °C for 2 h with  
 179 different solid state loadings: (A, a) 50 wt. %, (B, b) 55 wt. %, (C, c) 60 wt. %, at a fixed air-gap distance  
 180 of 15 cm and tap-water as external coagulant, respectively.

181 With ceramic suspensions consisting of 50 wt. %, 55 wt. % and 60 wt. % solid state  
 182 loadings, the spinel-based HFCMs were wet-dry and spun at an air gap distance of 15 cm and  
 183 a fixed bore fluid rate of 20 mL·min<sup>-1</sup>, followed by sintering at 1250 °C for 2 h. Cross sectional  
 184 SEM images of the fiber membranes are shown in **Fig. S7**. An asymmetric sandwich porous  
 185 structure was formed for all the spinel hollow fiber membranes with inner and outer finger-like  
 186 macro-void structures enhancing permeability and with sponge-like region providing the  
 187 majority of the mechanical strength and size-exclusion separation function (Zhu et al., 2016).  
 188 However, deformation of the lumen was observed when the ceramic loading was 50 wt. % (**Fig.**  
 189 **S7A**). With further increasing the ceramic loading to 55 wt. % (**Fig. S7B**) and 60 wt. % (**Fig.**  
 190 **S7C**), both fibers have regular inner and outer shape. When comparing the cross-sectional SEM  
 191 images of fiber2 and fiber3, a structure with much longer and bigger inner finger-like macro-  
 192 voids is observed for fiber3, while the thickness of outer finger-like macro-voids and sponge-  
 193 like region is reduced. This indicates that solid-state loadings play a crucial role in the formation  
 194 of regular lumen as well as the distribution and ratio of finger-like macro-voids and sponge-  
 195 like regions. When increasing solid state loadings, the viscosity of spinning suspension was

196 improved (Luiten-Olieman et al., 2011), which lowered the exchange rate of solvent and non-  
197 solvent. As a result, the formation of outer finger-like structure was suppressed and thinner  
198 outer finger-like macro-voids were observed, shown in Fig. S7c.

### 199 S3.2. Effect of air-gap distance



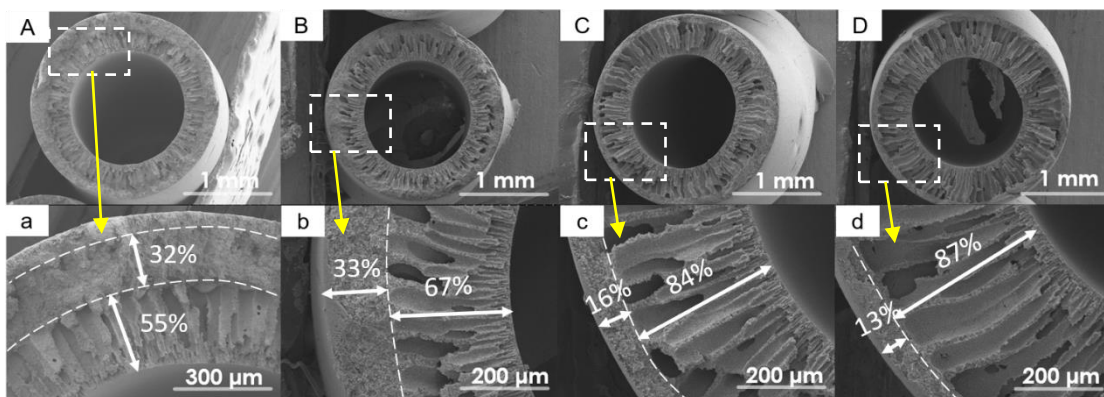
200  
201 **Fig. S8.** Cross sectional SEM images of fibers 3, 4 and 5 sintered at 1250 °C for 2 h with different air  
202 gap distances: (A, a) 3 cm, (B, b) 10 cm, (C, c) 15 cm, at a fixed solid-state loading of 60 wt. % and tap-  
203 water as the external coagulant, respectively.

204 **Fig. S8** shows spinel-based HFCMs spun with air gap distances of 3 cm, 10 cm and 15 cm,  
205 a solid-state loading of 60 wt. % and a fixed bore fluid rate of 20 mL·min<sup>-1</sup>, followed by  
206 sintering at 1250 °C for 2 h. All fibers have a structure consisting of a sponge-like region as  
207 well as the inner and outer finger-like macro-voids. However, the distribution and ratio of  
208 finger-like macro-voids and sponge-like regions varied with the air gap distances. With the  
209 increase of air gap distance, the thickness of the sponge-like region was gradually decreased,  
210 while the length of the inner finger-like macro-voids increased significantly (Kingsbury et al.,  
211 2010; Kingsbury and Li, 2009). When the fiber was spun into a non-solvent bath (tap water)  
212 with 3 cm air-gap distance (**Fig. S8a**), the finger-like macro-voids extend from the inner fiber  
213 surface across approximately 38% of the fiber cross-section, which is much longer than finger-  
214 like macro-voids originating from the outer fiber surface with only 12%. A central sponge-like

215 region between the inner and outer finger-like voids was estimated to be about 50% of the fiber  
216 cross-section.

217 The size and length of macro-voids at the inner edge are further increased when the air-gap  
218 distance is increased to 10 cm, the finger-like voids extended from the inner surface across  
219 approximately 50% of the fiber cross-section, while the sponge-like region was reduced, only  
220 occupying about 35% of the fiber cross-section (Fig. S8b). The thickness of sponge-like region  
221 (20%) between the inner and outer finger-like voids are further reduced when the air-gap  
222 distance is increased to 15 cm (Fig. S8c). When the fiber was extruded from the spinneret, rapid  
223 precipitation at the inner fiber walls occurred, resulting in long finger-like voids, before it was  
224 immersed in non-solvent coagulation bath. Therefore, the increase of air-gap induced more  
225 rapid precipitation, which occurred at the inner fiber walls and the presence of ambient moisture  
226 in the air caused an increase in viscosity at the outer surface of the fiber, which inhibit the  
227 formation of outer finger-like macro-voids and favor the growth of inner finger-like pores  
228 (Meng et al., 2016).

### 229 S3.3. Effect of external coagulant



230  
231 **Fig. S9.** Cross sectional SEM images of fibers 3, 6 and 8 prepared with different volumes of ethanol as  
232 external coagulants: (A, a) 0 vol%, (B, b) 30 vol%, (C, c) 60 vol%, (D, d) 90 vol% at a fixed air-gap  
233 distance of 15 cm and solid-state loading of 60 wt. %, respectively.

234 To investigate the effect of external coagulants on fiber morphology, different volumes of  
235 ethanol/water mixture solutions were used as external coagulants, with other conditions being

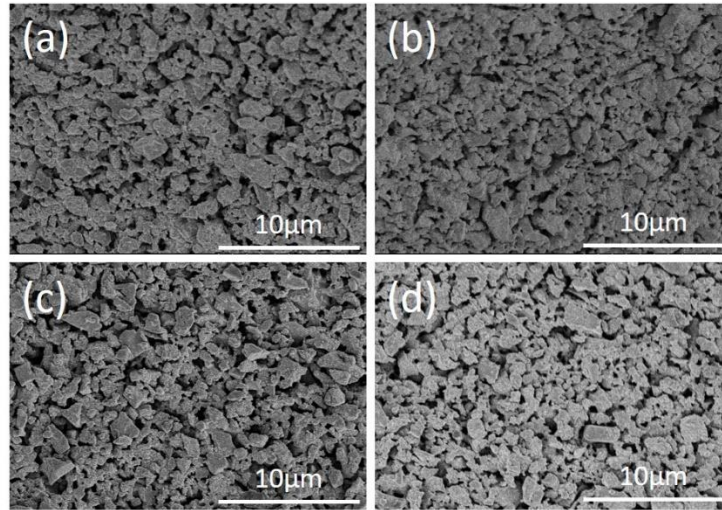


236 the same. The inner and outer finger-like macro-voids of the fiber prepared with water as the  
237 external coagulant account for approximately 55% and 13% of the fiber cross-section  
238 respectively (Fig. S9a), with the remaining 32% consisting of a sponge-like region. Addition of  
239 30 vol. % of ethanol into the external coagulants results in an increase in finger-like macro-  
240 voids which occupy 67% of the fiber cross-section (Fig. S9b). Although the thickness of the  
241 sponge-like region was not reduced, the finger-like voids appeared to migrate toward to the  
242 outer surface. With a further increase of volume percent of ethanol up to 60% and above, the  
243 cross-section of the fiber precursors are mainly composed of long and large inner finger-like  
244 macro-voids and thin sponge-like region, along with the elimination of outer finger-like macro-  
245 voids (Figs. S9c and S9d). A similar phenomenon has been also reported by Zhang et al. (Zhang  
246 et al., 2015), who prepared the YSZ hollow fibers with ethanol as external coagulant and finger-  
247 like macro-voids extended from the inner wall across approximately 90% of the fiber cross-  
248 section. These differences in microstructure of the fiber precursor could be attributed to the  
249 coagulation power of coagulant which influenced the cross-section structure formation of  
250 membranes significantly during phase inversion process. As the coagulation power increases,  
251 the polymer-solvent interaction is enhanced, and thus the precipitation rate is improved to form  
252 finger-like structures (Um et al., 2004). Compared with water, ethanol is a weak coagulant.  
253 Thus, when more ethanol was incorporated as the external coagulant, the precipitation of  
254 polymer was significantly inhibited at the outer surface of the fiber. In addition, using strong  
255 coagulant water as the internal coagulant at the inner side of the nascent fibers leads to the rapid  
256 precipitation of polymer. The presence of an air-gap distance of 15 cm further promotes  
257 extending the finger-like macro-voids toward to the outer side (Um et al., 2004; Wang et al.,  
258 2000). Thus, a structure with long and large finger-like macro-voids and a thin sponge-like  
259 region is formed.

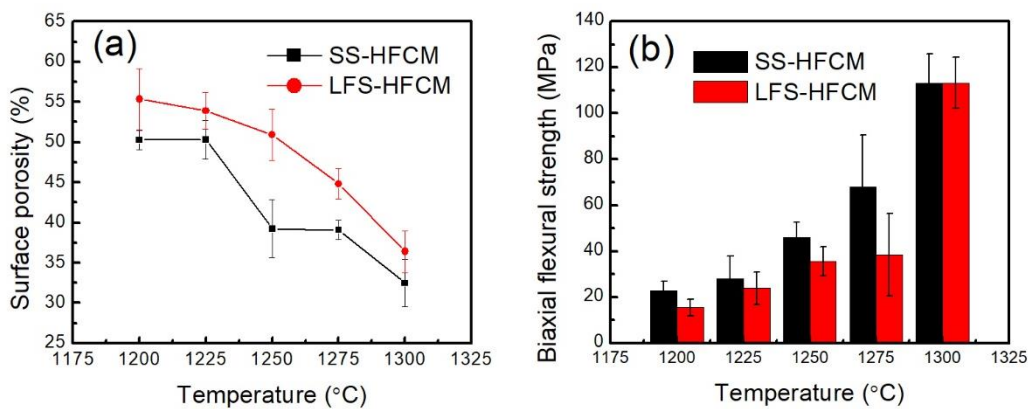
260 Compared with the hollow fibers prepared using water as the external coagulant (sandwich



261 structured HFCM (SS-HFCM), fiber 3), the highly asymmetric hollow fibers having long  
 262 finger-like pore structured HFCM (LFS-HFCM) (fiber 7) prepared with 60% volume of ethanol  
 263 as external coagulant are more beneficial for the development of separation membranes as the  
 264 thin outer sponge-like region reduces mass transfer resistance effectively during the filtration  
 265 process (Burggraaf, 1996).



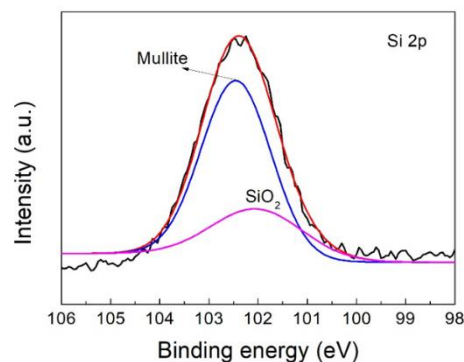
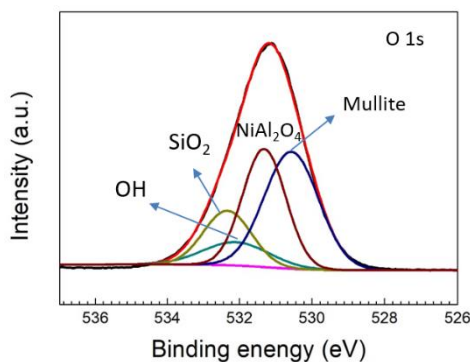
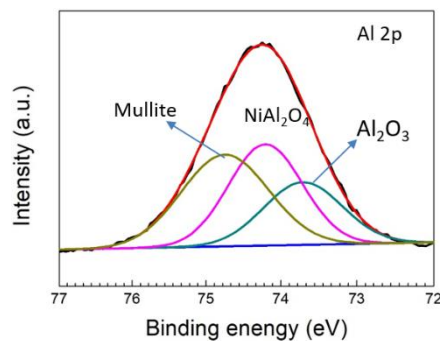
266  
 267 **Figure. S10.** Inner and outer surface SEM images of SS-HFCM and LFS-HFCM sintered at 1250 °C:  
 268 (a) inner surface of SS-HFCM, (b) outer surface of SS-HFCM, (c) inner surface of LFS-HFCM, (d)  
 269 outer surface of LFS-HFCM.



270  
 271 **Fig. S11.** (a) Surface porosity and (b) biaxial flexural strength of SS-HFCM and LFS-HFCM sintered  
 272 from 1200 to 1300 °C

273 **Fig. S11** shows the surface porosity and mechanical strength of SS-HFCM and LFS-HFCM

274 after sintering at various temperatures (1200-1300 °C). The surface porosity of SS-HFCM and  
 275 LFS-HFCM both decrease with sintering temperature, while LFS-HFCM always has a higher  
 276 surface porosity than SS-HFCM. A reverse phenomenon was observed for the bending strength  
 277 of both fibers, which increases with the sintering temperatures. SS-HFCM always has a higher  
 278 strength than LFS-HFCM, except at 1300 °C. As the sponge-like regions provide the majority  
 279 of the mechanical strength of hollow fiber membranes, SS-HFCM has a thicker sponge-like  
 280 region than LFS-HFCM and a higher mechanical strength is observed for SS-HFCM. When the  
 281 sintering temperature increases up to 1300 °C, a severe densification process occurs, resulting  
 282 in a dramatic increase in mechanical strength for both fibers, which is independent of the fiber  
 283 structures.



284  
 285 **Fig. S12.** XPS spectra of O 1s, Al 2p and Si 2p of LFS-HFCM sintered at 1250 °C

286 **S4 Oil-in-water emulsion separation**

287 *S4.1. Introduction of membrane fouling models*

288 To analyze cross-flow microfiltration flux decline profiles of O/W emulsions, four fouling

289 models, namely cake filtration model, intermediate pore blocking, standard pore blocking  
290 model and complete pore blocking model have been used (Kumar et al., 2015; Vasanth et al.,  
291 2013; Salahi et al., 2010; Nandi et al., 2010). The cake filtration model is applied to the situation  
292 where particles larger than the average pore size deposit on the membrane surface, thus forming  
293 a cake filtration layer, which provide an additional porous barrier to the permeating liquid.  
294 Intermediate pore blocking occurs when the solute particle sizes are equivalent to the membrane  
295 pore sizes. Using this model, the membrane pores are considered as not necessarily blocked by  
296 the solute particles. Standard pore blocking is caused by the non-uniformity of pore paths and  
297 pore blocking inside the membrane pore occurs when the solute particle sizes are smaller than  
298 the membrane pores. In complete pore blocking, the sizes of solute particle are bigger than the  
299 membrane pore and thus pore blocking usually occurs on the membrane surface rather than  
300 within the membrane pore. The four fouling models are expressed by the following linearized  
301 equations of the membrane flux (J) and time (t) (Hermia, 1982):

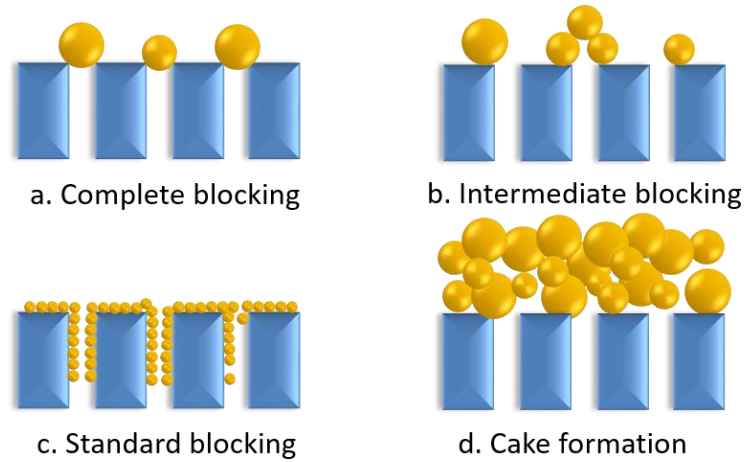
302 (a) Cake filtration:  $J^{-2} = J_0^{-2} + k_c t$  (3)

303 (b) Intermediate pore blocking:  $J^{-1} = J_0^{-1} + k_i t$  (4)

304 (c) Standard pore blocking:  $J^{-0.5} = J_0^{-0.5} + k_s t$  (5)

305 (d) Complete pore blocking:  $\ln (J^{-1}) = \ln (J_0^{-1}) + k_b t$  (6)

306 The fitting of the experimentally acquired permeate flux decline vs time data with any of  
307 above models is confirmed by comparing the coefficient of correlation ( $R^2$ ) values coupled with  
308 positive combinations of slope and intercept values obtained from linear fit analysis. As a result,  
309 the model that represents experimental data with best fit  $R^2$  is considered to indicate the  
310 pertinent fouling mechanism during cross flow microfiltration.



311

312

**Fig. S13.** Illustration of fouling mechanisms considered by the models.

313 To explain the results in a better way, we also have calculated Reynolds number (Re) at

314 different cross-flow velocities (Table S7) using the following equation:

$$315 \quad \text{Re} = \rho v d / \mu \quad (7)$$

316 Where  $\rho$  is the density of the fluid ( $\text{kg} \cdot \text{m}^{-3}$ ),  $v$  is the velocity of the fluid with respect to the

317 object ( $\text{m} \cdot \text{s}^{-1}$ ),  $d$  is the inner diameter of the membrane tube (m), and  $\mu$  is the dynamic viscosity

318 of the fluid ( $\text{kg} \cdot \text{m}^{-1} \cdot \text{s}^{-1}$ ).

319 **Table S6**

320 Summary of parameters associated with various pore blocking models at different cross-flow

321 velocities for O/W emulsion separation.

membrane	Cross -flow veloc ity ( $\text{m} \cdot \text{s}^{-1}$ )	Cake filtration			Intermediate pore blocking			Standard pore blocking		Complete pore blocking			
		$R^2$	$k_c$ ( $\text{s} \cdot \text{m}^{-2}$ )	$J_0^{-2 \times}$ $10^{-7}$	$R^2$	$k_i$ ( $\text{m}^{-1}$ )	$J_0^{-1 \times}$ $10^{-3}$	$R^2$	$k_s$ ( $\text{s}^{0.5} \cdot \text{m}^{0.5}$ )	$J_0^{0.5 \times}$ $10^{-1}$	$R^2$	$k_b$ ( $\text{s}^{-1}$ )	$\ln(J_0^{-1})$
LFS-HFCM	0.56	0.966	0.318	13.78	0.934	0.089	12.46	0.907	0.034	11.26	0.874	0.005	9.46
LFS-HFCM	1.12	0.988	0.248	5.03	0.955	0.091	8.27	0.925	0.039	9.25	0.887	0.007	9.08
LFS-HFCM	1.67	0.973	0.055	1.86	0.968	0.038	4.76	0.961	0.023	6.99	0.949	0.005	8.51

322

323 **Table S7**

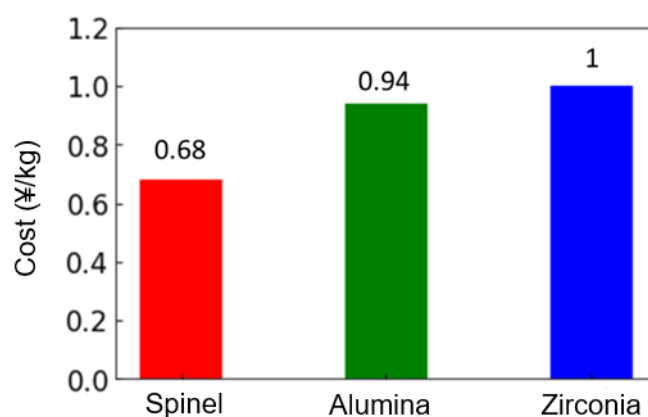
324 Reynolds number at different cross-flow velocities.

Cross-flow velocity (m·s <sup>-1</sup> )	Reynolds number (Re)	Flow patterns
0.56	728	Laminar flow
1.12	1456	Laminar flow
1.67	2171	Laminar–turbulent transition

---

325

326 *S4.2. Cost and environmental risk assessment*



327

328 **Fig. S14.** Comparison of membrane fabrication cost based on consumption of raw materials and  
 329 electricity during sintering.

330 The sintering temperature of spinel-based HFCMs in this study is much lower than of  
 331 traditional ceramic membranes such as Al<sub>2</sub>O<sub>3</sub> and ZrO<sub>2</sub>. The cost analysis is based on the raw  
 332 materials and energy consumption for membrane sintering. The spinel-based HFCMs has a  
 333 lower fabrication cost than Al<sub>2</sub>O<sub>3</sub> and ZrO<sub>2</sub> membranes due to cheaper raw materials and lower  
 334 sintering temperatures. The stabilization cost using bauxite as precursors is also lower than  
 335 those using alumina and kaolinite as precursors. Therefore, bauxite is a promising candidate  
 336 raw material for both heavy-metal stabilization and membrane fabrication due to lower cost and  
 337 outstanding separation performance in water treatment.

338

339 **Table S8**

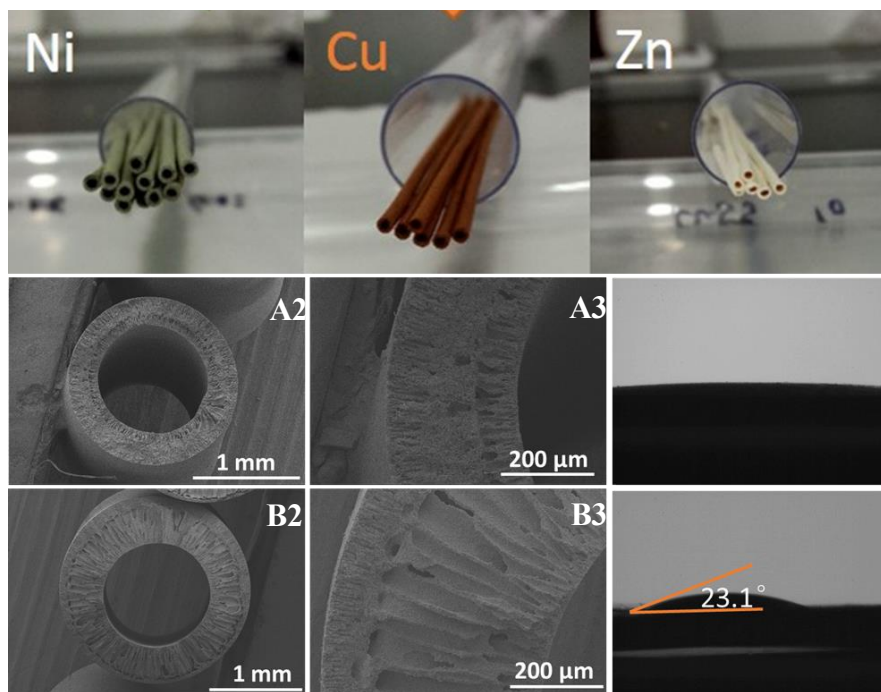
340 The concentrations of some typical metal-ions in the permeate after membrane separation  
341 operation of oil-in-water emulsion

Concentration ( $\mu\text{g}\cdot\text{L}^{-1}$ )	Al	Ca	Fe	K	Mg	Na	Ni	Ti
This work	13.7	77.1	---	69.4	14.6	144.7	0.7	---
Drinking water criterion (WHO)	900	-	0.3	-	-	5000	70	-

342 --- non-detected

343

344 **S5. Preliminary extension to other spinel systems**



345

346 **Fig. S15.** Photos of NiAl<sub>2</sub>, CuAl<sub>2</sub> and ZnAl<sub>2</sub> hollow fiber ceramic membranes and cross sectional SEM  
347 images CuAl<sub>2</sub> (A1, A2) and ZnAl<sub>2</sub> (B1, B2) sintered at 1000 °C and 1400 °C for 2 h respectively, (A3)  
348 water contact angle of CuAl<sub>2</sub> sintered at 1000 °C and (B3) water contact angle of ZnAl<sub>2</sub> sintered at

349 1400 °C.

350

351 The study of recycling of nickel-laden wastewater sludge for rational fabrication of spinel-  
352 based ceramic membranes is not only an efficient way to highly efficiently stabilize heavy  
353 metals in wastewater sludge into much more stable spinel phase, but also to provide a new  
354 avenue for developing high performance robust membranes for water treatment. Furthermore,  
355 this strategy is not limited to nickel and could also extend to other heavy metals in wastewater  
356 sludge such as copper and zinc. The CuAl<sub>2</sub> and ZnAl<sub>2</sub> membranes prepared via the protocol  
357 proposed in this study also show a good asymmetric structure and have a water contact angle  
358 of 0° and 21°, respectively (Fig. S15), indicating a great potential for water treatment due to  
359 their excellent hydrophilicity.

360

361 **References**

- 362 Burggraaf, A.J., 1996. Membrane Science and Technology, pp. 21-34, Elsevier.
- 363 Dong, Y., Hampshire, S., Lin, B., Ling, Y. Zhang, X., 2010. High sintering activity Cu–Gd co-doped  
364 CeO<sub>2</sub> electrolyte for solid oxide fuel cells. *J. Power Sources* 195 (19), 6510-6515.
- 365 Hermia, J., 1982. Constant pressure blocking filtration laws-application to power-law non-Newtonian  
366 fluids. *Chem. Eng. Res. Des.* 60, 183-187.
- 367 Kingsbury, B.F., Li, K., 2009. A morphological study of ceramic hollow fiber membranes. *J. Membr.*  
368 *Sci.* 328 (1-2), 134-140.
- 369 Kingsbury, B.F., Wu, Z., Li, K., 2010. A morphological study of ceramic hollow fiber membranes: A  
370 perspective on multifunctional catalytic membrane reactors. *Catal. Today* 156 (3-4), 306-315.
- 371 Kumar, R.V., Ghoshal, A.K., Pugazhenti, G., 2015. Elaboration of novel tubular ceramic membrane  
372 from inexpensive raw materials by extrusion method and its performance in microfiltration of  
373 synthetic oily wastewater treatment. *J. Membr. Sci.* 490, 92-102.
- 374 Li, L., Dong, X., Dong, Y., Zheng, Y.-M., Zhu, L., Liu, J., 2015a. Thermal conversion of hazardous  
375 metal copper via the preparation of CuAl<sub>2</sub>O<sub>4</sub> spinel-based ceramic membrane for potential  
376 stabilization of simulated copper-rich waste. *ACS Sustain. Chem. Eng.* 3 (11), 2611-2618.
- 377 Li, L., Dong, X., Dong, Y., Zhu, L., You, S.-J., Wang, Y.-F., 2015b. Incorporation of zinc for fabrication  
378 of low-cost spinel-based composite ceramic membrane support to achieve its stabilization. *J. Hazard.*  
379 *Mater.* 287, 188-196.
- 380 Luiten-Olieman, M.W., Winnubst, L., Nijmeijer, A., Wessling, M., Benes, N.E., 2011. Porous stainless  
381 steel hollow fiber membranes via dry–wet spinning. *J. Membr. Sci.* 370 (1-2), 124-130.
- 382 Meng, X., Liu, Z., Deng, C., Zhu, M., Wang, D., Li, K., Deng, Y., Jiang, M., 2016. Microporous nano-  
383 MgO/diatomite ceramic membrane with high positive surface charge for tetracycline removal. *J.*  
384 *Hazard. Mater.* 320, 495-503.
- 385 Nandi, B., Moparthy, A., Uppaluri, R., Purkait, M., 2010. Treatment of oily wastewater using low cost  
386 ceramic membrane: comparative assessment of pore blocking and artificial neural network models.  
387 *Chem. Eng. Res. Des.* 88 (7), 881-892.
- 388 Salahi, A., Gheshlaghi, A., Mohammadi, T., Madaeni, S.S., 2010. Experimental performance evaluation  
389 of polymeric membranes for treatment of an industrial oily wastewater. *Desalination* 262 (1-3), 235-  
390 242.
- 391 Shih, K., Tang, Y., 2011. Prolonged toxicity characteristic leaching procedure for nickel and copper  
392 aluminates. *J. Environ. Monitor.* 13 (4), 829-835.
- 393 Shih, K., White, T., Leckie, J.O., 2006a. Nickel stabilization efficiency of aluminate and ferrite spinels  
394 and their leaching behavior. *Environ. Sci. Technol.* 40 (17), 5520-5526.
- 395 Shih, K., White, T., Leckie, J.O., 2006b. Spinel formation for stabilizing simulated nickel-laden sludge  
396 with aluminum-rich ceramic precursors. *Environ. Sci. Technol.* 40 (16), 5077-5083.
- 397 Tang, Y., Chui, S.S.-Y., Shih, K., Zhang, L., 2011a. Copper stabilization via spinel formation during the



398 sintering of simulated copper-laden sludge with aluminum-rich ceramic precursors. *Environ. Sci.*  
399 *Technol.* 45 (8), 3598-3604.

400 Tang, Y., Shih, K., Wang, Y., Chong, T.-C., 2011b. Zinc stabilization efficiency of aluminate spinel  
401 structure and its leaching behavior. *Environ. Sci. Technol.* 45 (24), 10544-10550.

402 Um, I.C., Kweon, H., Lee, K.G., Ihm, D.W., Lee, J.-H., Park, Y.H., 2004. Wet spinning of silk polymer:  
403 I. Effect of coagulation conditions on the morphological feature of filament. *Int. J. Biol. Macromol.*  
404 34 (1-2), 89-105.

405 Vasanth, D., Pugazhenthii, G., Uppaluri, R., 2013. Cross-flow microfiltration of oil-in-water emulsions  
406 using low cost ceramic membranes. *Desalination* 320, 86-95.

407 Wang, D., Li, K., Teo, W., 2000. Highly permeable polyethersulfone hollow fiber gas separation  
408 membranes prepared using water as non-solvent additive. *J. Membr. Sci.* 176 (2), 147-158.

409 Zhang, X., Hu, J., Chang, Q., Wang, Y., Zhou, J.-e., Zhao, T., Jiang, Y., Liu, X., 2015. Influences of  
410 internal coagulant composition on microstructure and properties of porous YSZ hollow fibre  
411 membranes for water treatment. *Sep. Purif. Technol.* 147, 337-345.

412 Zhu, L., Chen, M., Dong, Y., Tang, C.Y., Huang, A., Li, L., 2016. A low-cost mullite-titania composite  
413 ceramic hollow fiber microfiltration membrane for highly efficient separation of oil-in-water  
414 emulsion. *Water Res.* 90, 277-285.

415

416